Lifetime Experiments of Regeneratively Cooled Rocket Combustion Chambers and PIV Measurements in a High Aspect Ratio Cooling Duct

Felix Hötte, Oliver Günther, Christoph von Sethe, Matthias Haupt, Peter Scholz, and Michael Rohdenburg

Abstract This paper aims at experimental investigations of the life limiting mechanisms of regeneratively cooled rocket combustion chambers, especially the so called doghouse effect. In this paper the set up of a cyclic thermo-mechanical fatigue experiment and its results are shown. This experiment has an actively cooled fatigue specimen that is mounted downstream of a subscale GOX-GCH_4 combustion chamber with rectangular cross section. The specimen is loaded cyclically and inspected after each cycle. The effects of roughness, the use of thermal barrier coatings, the length of the hot gas phase, the oxygen/fuel ratio and the hot gas pressure are shown. In a second experiment the flow in a generic high aspect ratio cooling duct is measured with the Particle Image Velocimetry (PIV) to characterize the basic flow. The main focus of the analysis is on the different recording and processing parameters of the PIV method. Based on this analysis a laser pulse interval and the window size for auto correlation is chosen. Also the repeatability of the measurements is demonstrated.

F. Hötte (✉) · M. Haupt · M. Rohdenburg
TU Braunschweig, Institute of Aircraft Design and Lightweight Structures, Hermann-Blenk-Str. 35, 38108 Braunschweig, Germany
e-mail: f.hoette@tu-braunschweig.de

M. Haupt
e-mail: m.haupt@tu-braunschweig.de

M. Rohdenburg
e-mail: m.rohdenburg@tu-braunschweig.de

O. Günther · P. Scholz
TU Braunschweig, Institute of Fluid Mechanics, Hermann-Blenk-Str. 37, 38108 Braunschweig, Germany
e-mail: o.guenther@tu-bs.de

P. Scholz
e-mail: p.scholz@tu-bs.de

C. von Sethe
TU Munich, Chair of Turbomachinery and Flight Propulsion, Boltzmannstraße 15, 85748 Garching, Germany
e-mail: christoph.sethe@tum.de

N. A. Adams et al. (eds.), *Future Space-Transport-System Components under High Thermal and Mechanical Loads*, Notes on Numerical Fluid Mechanics and Multidisciplinary Design 146, https://doi.org/10.1007/978-3-030-53847-7_18

These results are the starting point for future measurements on the roughness effect on heat transfer and pressure loss in a high aspect ratio cooling duct.

1 Introduction

Regeneratively cooled rocket combustion chambers have to resist extreme harsh environment conditions. These are the very high temperature level of the hot gas, extreme temperature gradients and pressure differences between coolant and hot gas, the reactive hot gas composition and abrasive flow. For the demand to increase the thrust-to-weight ratio, the lifetime, the safety and to reduce the costs a detailed knowledge of the life-limiting mechanisms is mandatory. Since numerical lifetime predictions are not well-engineered currently, these mechanisms have to be studied mainly on experiments.

For lifetime investigations of regeneratively cooled rocket combustion chamber structures a sub scale experiment was designed and conducted. A modular test section is placed downstream of a 5-injector sub scale combustion chamber with rectangular cross section. The test section houses a replaceable fatigue specimen with 17 high aspect ratio cooling channels. The specimen is loaded cyclically and inspected after each cycle.

In the past some experiments on cylindrical sub scale combustion chamber structures were conducted, for example see [4, 10, 13]. The deformations of the hot gas wall were not investigated quantitatively. The coolant's flow was not regulated or measured individually for each cooling channel. In other experiments flat specimens were investigated, in which the hot gas flow was replaced by laser irradiation, for example see [15].

The novel approach presented in this paper is the use of a rectangular cross section and a replaceable specimen with individually controlled cooling flow through the cooling channels combined with the hot gas flow. This leads to the possibility of detailed deformation and roughness inspections under well defined and realistic conditions. Because of that the results can be used also for validation of numerical simulations.

In comparison to the previous test campaigns A and B, which are described in detail in [9], in the actual campaigns C-K a much more stable combustion could be achieved. In campaigns C-G the combustion chamber pressure was increased slightly to accelerate the thermo-mechanical fatigue by higher temperatures and heat fluxes, whereas the cooling conditions were not changed. In campaigns C and D the default design of the fatigue specimen were tested, whereas in campaign E a fatigue specimen with a higher initial surface roughness was used. In campaigns F and G fatigue specimens with thermal barrier coatings were tested. In campaigns H-K the hot gas pressure and the coolant mass flow were increased by 50 %. In addition, the burning times and oxygen to fuel ratios were varied. Further details about campaigns C-K are given in [16].

Not only the fluid structure interaction of the hot gas flow but also the design of the cooling ducts plays an important role for the lifetime prediction of combustion chambers. The pressure loss and the heat transfer are the main aspects of the cooling ducts. The roughness and surface imperfections of the ducts wall both have a great influence on them. With new additively manufacturing technologies this design aspect gets even more important. Therefore a detailed roughness study should be performed at high Reynolds numbers.

Previous studies were often done at low Reynolds numbers or were just providing integral data. Also in most experiments additional roughness elements like grooves or ribs are used, for example see [1–3]. Other experiments investigated a fully turbulent high aspect ratio duct flow with smooth and rod-roughened walls using hot-wire anemometry, but don't provide any information about the heat flux, see [12]. Investigations of the flow and the heat transfer in one sided heated cooling ducts have been carried out as well. However, they were focusing on triangular and rectangular ducts, providing only integral data of the heat transfer at lower Reynolds numbers, see [2, 3]. In further experiments with roughened tubes it was stated that the heat transfer is highly affected by the surface roughness [11] and studies in a triangular duct showed that the heat transfer coefficient can be increased with higher surface roughness using the same pumping power, see [14]. To better characterize the roughness effects on heat transfer and pressure loss locally resolved measurements of the flow field and the temperature field at high Reynolds numbers are needed.

In order to analyze the roughness effects a well known reference case with smooth walls is needed as well. In a preliminary measurement the pressure losses in a high aspect ratio cooling duct with one heated wall were determined and a measurement uncertainty quantification was performed [8]. Subsequently, particle image velocimetry was used to provide well known reference data. These analysis focus on the different recording and processing parameters.

In the following sections a description of the set-up of the fatigue experiment and its results are shown. The cooling duct experiment and the results are presented in Chap. 3. In the end a short conclusion is given.

2 Fatigue Experiment

2.1 Experimental Set-Up

For lifetime investigations of cooling channel structures under thermo-mechanical load a fatigue segment is placed downstream of a GOX-GCH_4 rectangular combustor at a characteristic length L* = 0.717 m, which is sufficient to achieve a complete combustion. A special aim is to reproduce the so called "doghouse" effect, a structural failure mode which is caused by thermo-mechanical load cycles.

The cross section of the combustion chamber has a width of 48 mm and a height of 12 mm. Figure 1a shows a cut view of the fatigue segment and visualizes the fluid

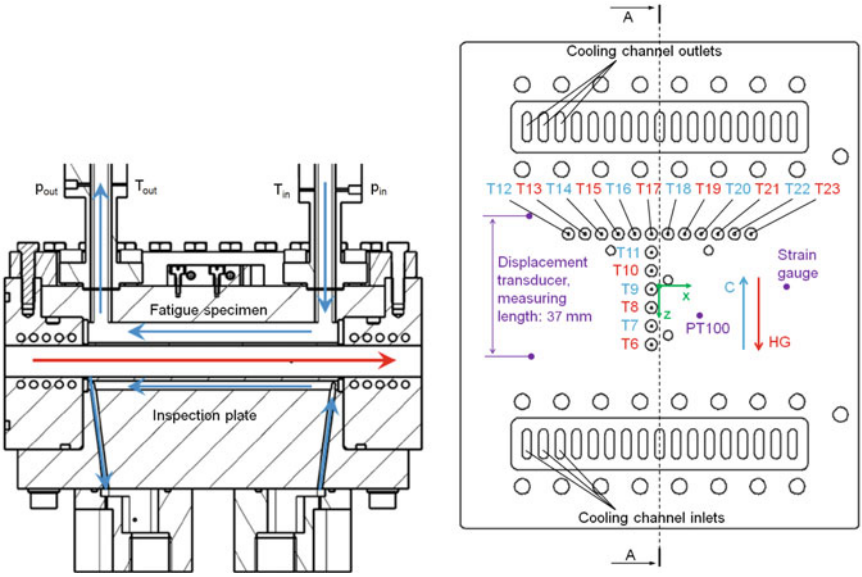

(a) Fatigue segment cut view (Reprinted by permission from Springer Nature [6]), cut position marked as A-A in Fig. 1(b)

(b) Fatigue specimen top view with flow directions and measurement positions (Reprinted by permission from Felix Hötte [9]

Fig. 1 Fatigue experiment set-up

flows (red for hot gas, blue for coolant). The injector elements are flush mounted. The fatigue segment houses a replaceable fatigue specimen made of copper alloy CuCr1Zr. The specimen is attached with a floating bearing which allows free thermal expansion. It has 17 rectangular cooling channels with a height of 8 mm, a width of 2.5 mm, a fin thickness of 2 mm and a length of 96 mm. The wall thickness between the surface exposed to the hot gas and the cooling channel bottom side is 1 mm. The specimen is loaded cyclically. One cycle consists of pre-cooling, 2-stage hot run and post-cooling phase. After each cycle the deformation of the specimen's hot gas wall is measured by a laser profile scanner. To access the hot gas surface without the need to disassemble the fatigue specimen, the water-cooled inspection plate on the opposite side is removed.

High pressure ambient temperature nitrogen is used as coolant for the specimen. To ensure well defined conditions in the three central cooling channels the mass flow rates here are closed loop controlled individually (PID). The coolant supply for the remaining 14 channels are separated in two closed loop controlled lines. The mass flow rates in each of these five supply lines is measured using a Coriolis flow meter located downstream of the fatigue specimen. Also the inlet pressure is regulated by a PID-control. The temperature and pressure of the coolant are measured in the inlet and outlet manifolds of the specimen in the 4., 8., 9., 10., and 14. cooling channel by thermocouples respectively pressure transducers (see Fig. 1a).

The specimen is equipped with several thermocouples in different positions and depths to measure the temperature distribution in the structure during each cycle. Figure 1b shows the top view of the fatigue specimen with the green coordinate system in the center. In addition, the thermocouple positions T6-T23 (red for 3 mm and blue for 5 mm hot gas distance) are shown. The most central located thermocouple T9 has the coordinates x = −2.25 mm / z = 1 mm. The thermocouples have a spacing of 5 mm in axial (in hot gas flow direction) and 4.5 mm in transversal (orthogonal to the hot gas flow) direction respectively. They are located in the symmetry planes of the fins and are pushed by spring constructions against the measurement locations in the eroded blind holes. The blue and red arrows indicate the flow directions of nitrogen (C) and hot gas (HG).

Furthermore, on the fatigue specimen upper surface a thermocouple (PT100, x = 11 mm / z = 8 mm) and a T-rosette strain gauge (x = 34 mm / z = 0) are placed. The axial elongation is measured by an inductive displacement transducer. This transducer is measuring between two cantilevers with a distance of 37 mm, which are fixed with bolts on the fatigue specimen's upper surface. The positions of the contact points of the transducer are marked in Fig. 1b (x = –35 mm / z = 18.5 mm respectively x = –35 mm / z = –18.5 mm).

The design process of the fatigue experiment is explained in [6].

2.2 Load Conditions

Table 1 shows a comparison of the load conditions of test campaigns B-K. While the initial low pressure stage lasts 7.5 s for all tests, the high pressure second stage lasts 20 s for campaigns B-G and K and only 10 s for campaigns H-J. The load conditions according to Table 1 show the values of the nominal stages. The ignition stages have approximately the same mixture ratios and half the chamber pressures. The duration of the post-cooling phase is controlled manually, but not stopped before the temperature in the specimen has fallen below 400 K.

2.3 Load Phases

During a load cycle the hot gas wall of the specimen has to resist three different life limiting phases. These phases are shown in Fig. 2 and described in the following:

1. Ignition and stage change (for 15 s< time < 17.6 s and 23 s < time < 24.2 s): After ignition respectively after stage change the temperature of the hot gas wall increases rapidly and the hot gas wall expands. The rest of the structure is still cold and restrains the hot gas wall expansion. Therefore, the hot gas exposed surface is bending convexly and the upper specimen surface is bending concavely. This decreases the measured elongation rapidly and the hot gas wall is loaded by very

Table 1 Load conditions in test campaigns B-K, averaged over all cycles

Campaign	Mixture ratio	Chamber pressure	Maximum temperature (T 17)	Number of cycle	Coolant mass flow rate per channel	Coolant pressure
B	3.87	17.2 bar	929 K	45	8 g/s	70 bar
C	3.92	19.0 bar	998 K	48	8 g/s	70 bar
D	3.94	19.2 bar	973 K	46	8 g/s	70 bar
E	3.87	19.1 bar	1020 K	16	8 g/s	70 bar
F	3.65	19.3 bar	983 K	1	8 g/s	70 bar
G	3.89	19.3 bar	975 K	36	8 g/s	70 bar
H	3.88	28.8 bar	1017 K	15	12 g/s	80 bar
I	3.95	28.7 bar	976* K	2	12 g/s	80 bar
J	3.42	28.7 bar	943 K	34	12 g/s	80 bar
K	3.41	28.5 bar	976 K	25	12 g/s	80 bar

*Because of a manufacturing error this value was measured 4.5 mm instead of 3 mm apart from the hot gas exposed surface

high in-plane compression stresses. In addition, the walls between coolant and hot gas bulge into the hot gas due to the large pressure difference. In combination with high temperatures and time, this leads to creeping. In this phase creeping can be neglected, because of its short time and the low temperature of the hot gas wall in comparison to the other phases.

2. Hot gas run (for 17.6 s < time < 23 s and 24.2 s < time < 43 s): Afterwards, the heat reaches the back parts of the structure and the thermal stresses are decreasing until a steady-state is reached (which is not reached in the tests). Because of the active cooling, the in-plane compression stresses in the hot gas wall would not reach zero during a steady-state. The bending decreases and the complete specimen expands thermally. Therefore, the measured elongation increases. In contrast to phase 1 and 3 creeping is important, since the thin hot gas wall has to resist high pressure differences between hot gas and coolant and compressive stresses due to the temperature difference for a long time, while it reaches temperatures above 1000 K. In addition, blanching, abrasion and thermal aging can be present in this phase.
3. Shutdown phase (for 43 s < time < 46 s): After shutdown the temperature of the hot gas wall decreases much faster than the rest of the structure, since it has a much lower heat capacity, and due to the high heat flux of the impinging coolant. This leads to very high in-plane tensile forces and a concave bending of the hot gas exposed surface, which rapidly increases the measured elongation on the upper side. In this phase creeping can be neglected, because of the quickly decreasing temperatures.

   For time > 46 s, the measured elongation decreases. This indicates, that the vertical temperature difference decreases, which reduces the bending of the specimen and

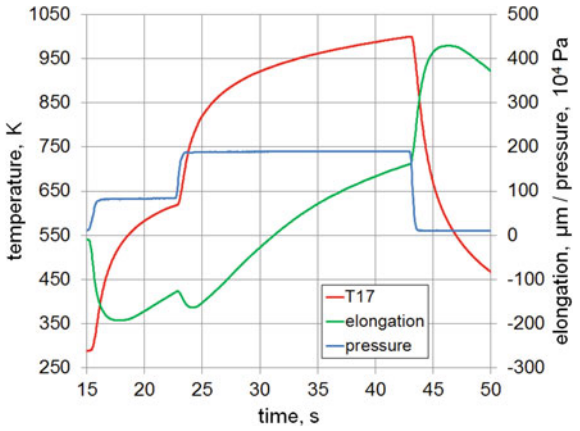

Fig. 2 Averaged temperature, elongation and hot gas pressure transients during campaign C

the in-plane tensile stresses. In addition, the temperature falls below 600 K, which increases the yield strength. Therefore, it is concluded, that the loading after 46 s can be neglected.

2.4 Deformations and Lifetime

A laser-profile-scanner is used to measure the profile of the deformed hot gas exposed surface 2 cm apart from the leading edge of the specimen in transverse direction. Figure 3a shows the profile at the end of test campaign C. The height of deformation d is defined as the difference of the global maximum and global minimum of the measured profile. Table 2 shows the initial mean roughness Ra on the hot gas exposed surface and the presence of thermal barrier coatings (see [7]) on the specimen. In addition, whether and why the specimen failed, the deformation height d at the end of each test campaign and its average increase per cycle is shown. Despite different load conditions, the doghouse effect (see Fig. 4) occurs repeatable, when d reaches around 40 µm. For test campaigns with low loading (B, C, D, G) the critical value is slightly higher (around 45 µm). The average slope of d depends strongly on the loading in terms of temperature gradient and level. In campaign G the slope of deformation is higher than in test campaign C, despite of similar load conditions. This indicates that the thermal barrier coating has reduced the lifetime. Probably, this is the consequence of the missing CuCr1Zr material, which was replaced by the thermal barrier coating (around 0.1 mm thickness).

Figure 3b shows the development of d during campaigns B, C, E, G, H, J and K. It is shown that the deformations increase nearly linearly with the number of cycles. The deformation development in campaign B is very erratic. It is assumed that this is a consequence of the combustion instabilities in some tests (see [9]. The

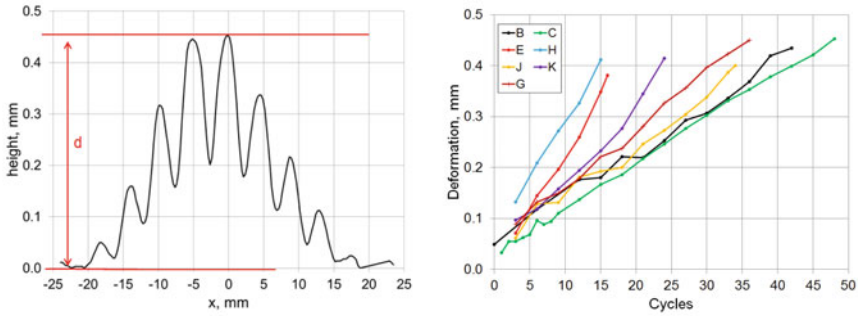

(a) Hot gas surface profile (b) Deformation d development

Fig. 3 Deformation measurement

Table 2 Initial and deformation properties of the specimen in test campaigns B-K

Campaign	Initial mean roughness	Special feature	Failure type	Final d µm	Average slope of d µm/cycle
B	< 0.5µm	/	/	46	1.02
C	< 0.5µm	/	Doghouse	45	0.94
D	< 0.5µm	/	Weld seam fracture	45	0.98
E	4 µm	/	Doghouse	38	2.38
F	< 0.5µm	TBC	TBC delamination	/	/
G	< 0.5µm	TBC	Weld seam fracture	45	1.25
H	2 µm	/	Doghouse	41	2.73
I	2 µm	/	Melting	/	/
J	2 µm	/	Doghouse	40	1.18
K	2 µm	/	/	41	1.71

comparison of campaigns C and E shows that a small increase of the hot gas heat flux (because of the higher roughness) decreases the lifetime by factor 3. In campaigns J and K the influence of the ignition and stage change phase can be assumed as equal, since the test conditions are very similar. The results of campaign A have shown that below wall temperatures of 850 K no deformations occur. Therefore, relevant creeping occurs only during the second load stage. In campaign K the duration of the second load stage is doubled in comparison to J and higher wall temperatures are reached. Therefore, creeping per cycle should be increased by more than factor 2. But the slope of deformation is only increased by 40%. Therefore, it is hypothesized that the influence of creeping on the lifetime is relatively small and the lifetime is mostly affected by the shutdown phase. Optical measurements of the remaining hot gas wall in campaign C have shown that abrasion has an insignificant influence (see

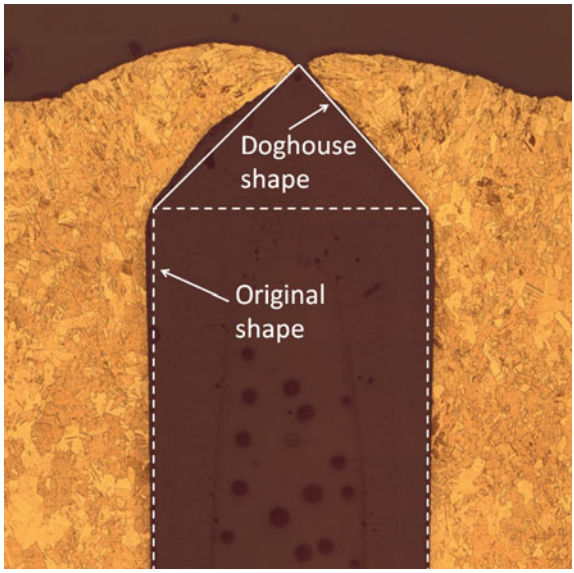

Fig. 4 Doghouse shape at the end of test campaign C

[8] for details). Thermal aging was investigated with micrographs after campaign B in [9]. No correlation between grain size distribution and temperature distribution was found.

3 Cooling Channel Measurements

3.1 Test Setup

For the flow characterization in a high aspect ratio cooling duct, we used a generic cooling duct facility with one heated wall. Regular tap water serving as the working fluid is stored in a tank. A centrifugal pump feeds the water through an electromagnetic flowmeter into the cooling duct and back to the tank. The mean flow rate and thus, the nominal bulk velocity u_b are controlled by the flowmeter. A second pump feeds the water from the tank into a cooling system to ensure a constant bulk temperature. A PT100 resistance temperature detector located at the outflow of the tank determines the bulk velocity.

Figure 5 shows a sketch of the generic cooling duct. The cooling duct has a nominal width of 6 mm and a nominal height of 25.8 mm. Thus, leading to an aspect ratio of 4.3 and a hydraulic diameter of 9.74 mm. The duct is made of PMMA to provide optical access. A heatable copper block with a tapered tip serves as the lower wall of the channel. Therefore it is possible to provide a heat flow from the wall into the working fluid. The duct is mounted on a heat barrier of PEEK, protecting the

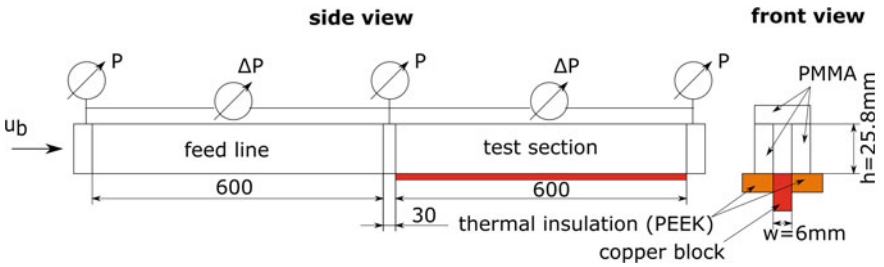

Fig. 5 Sketch of the experimental setup

PMMA from the high temperature of the copperblock. The length of the channel is 600 mm. A feed line in front of the test section ensures a fully developed turbulent flow. The feed line is geometrically equivalent to the test section, but the bottom wall is made from aluminum and is not heatable. A transition piece with a length of 30 mm connects the feed line and the test section. Also, in front of the feed line and at the end of the test section, transition pieces are attached. The rear transition piece also provides optical access from downstream into the test section.

The absolute pressure is measured at these three transition pieces. Additionally two differential pressure sensors were used to measure the pressure loss of the feed line and the test section separately, see Fig. 5.

We used Particle Image Velocimetry (2C2D-PIV) to provide detailed information about the mean velocity components and Reynolds stresses. Silver coated hollow glass spheres with a diameter of 10 µm served as tracer particles. A double-pulsed Nd-YAG solid-state laser operates as the light source. An optical lens system using a plano-concave lens with a focal length of −50 mm, a plano-convex lens with a focal length of +75 mm, and a concave cylindrical lens with a focal length of -50 mm forms the light sheet. It was arranged parallel to the direction of the mean flow, capturing the height of the duct. Widthwise it was located in the symmetric plane. The light sheet was directed into the test section from downstream into the test section resulting in fewer reflections on the bottom side of the duct. All the relevant degrees of freedom of the light sheet were aligned using micrometer screws and the Linos micro bench system. The light sheet thickness was adjusted to as small as possible. Using thermal sensitive paper and a digital caliper the thickness could be determined to 0.7 mm. However, due to the Gaussian distribution of the light, it does not necessarily have to be the true light section thickness. A long-distance microscope was used as a camera objective to ensure a high spatial resolution.

3.2 Light Sheet Alignment

To check the repeatability and the alignment of the laser light sheet four measurements have been carried out. First the laser sheet was aligned in the symmetry plane

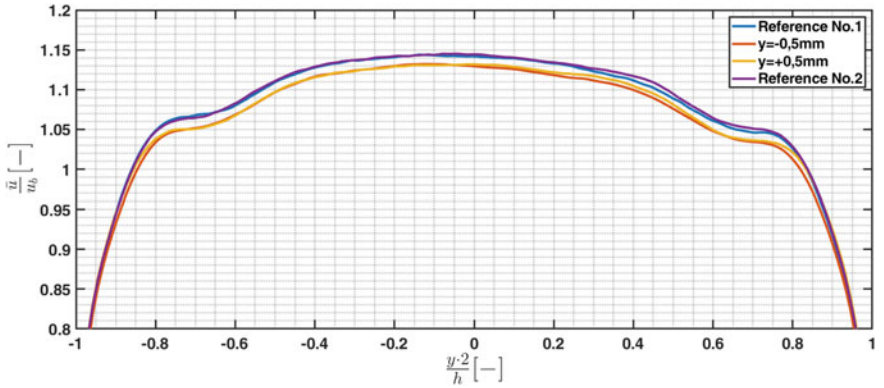

Fig. 6 Mean velocity profiles along the non-dimensional height of the duct, at different widthwise positions

of the duct using the micrometer screws. At this position data has been recorded as a reference measurement. Then the light sheet was moved in both directions by 0.5 mm from the center towards the sidewalls of the duct. At the end a second reference measurement was performed in the symmetry plane of the duct again. All movements were done with the micrometer screws of the light sheet optic. Figure 6 shows the mean velocity profiles of these measurements. Both the two reference measurements in the center and the two displaced measurements each coincide well. Two conclusions can be drawn from this. First, the repeatability of the alignment of the laser sheet is very accurate due to the micrometer screws. Also the measurements itself provide repeatable results. Second, the initial alignment of the laser light sheet was centered, which results from the fact that the flow pattern are symmetrical. It can also be seen, that a misalignment of 0.5 mm from the center of the duct, leads to a maximum error of 1.11% in the mean velocity.

3.3 Window Size Analysis

Another aspect of the analysis was the window size used for calculating the auto-correlation in the PIV post process. Different window sizes in the range of 16 px × 16 px to 96 px × 96 px has been used to calculate the vector fields. Due to the Gaussian distribution of the light sheet, particles that are in the center shine brighter than particles that are in the outer regions of the light sheet. To also analyze the effect of the light sheet thickness to filters with different threshold values were applied to the raw particle image. This filter removes all particles whose brightness is below the threshold value, narrowing the light sheet thickness artificially, but increasing the noise because the particle density decreases. Figure 7 shows the maximum velocity in the center of the duct over the window size for both the normal and the

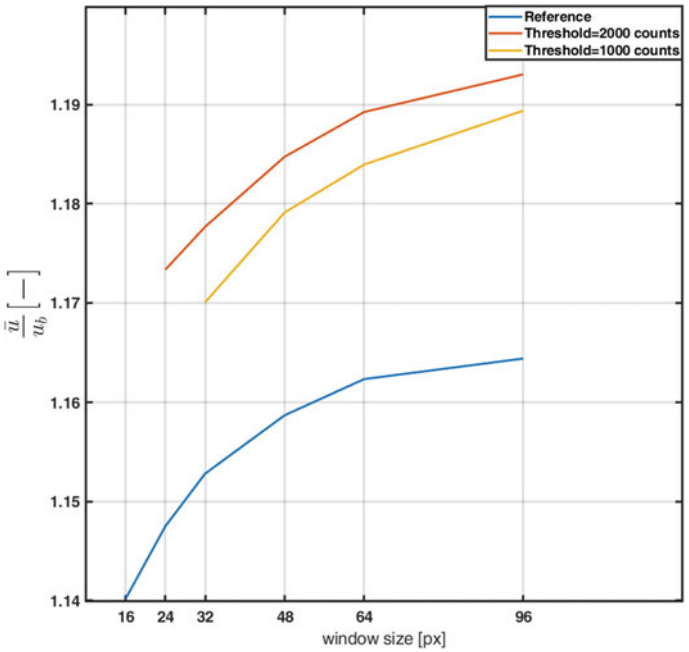

Fig. 7 Velocity in the center of the duct processed with different window sizes

filtered solution. It can be seen that the velocity rises with increasing window size showing asymptotic behavior. However, the differences are below 1 %. For window sizes below 48 px × 48 px the signal to noise ratio becomes low, and the results are noisy. With this results a window size of 64 px × 64 px has been chosen as the best trade-off between signal to noise ration and spatial resolution. As expected, the filtered solutions show higher velocities. The filter removes the slower particles in the outer regions of the light sheet, so the outer regions have less influence on the solution. The velocity difference is up to 2.3% with the chosen filters. This effect shows that with the relative thick light sheet referred to the small width of the channel, the results are smeared. Nevertheless, the use of these filters is only recommended to a limited extend, because the lower particle density leads to more spurious vectors and thus to higher measurement uncertainties. With averaging over more particle images, the uncertainties can possibly lowered to overcome the drawbacks.

3.4 Particle Shift

Four, respectively, three measurements have been done at two different Reynolds numbers to estimate the influence of the pixel shift. For both cases, the laser pulse interval Δt was varied between 5 µs and 24 µs resulting in different particle shift in

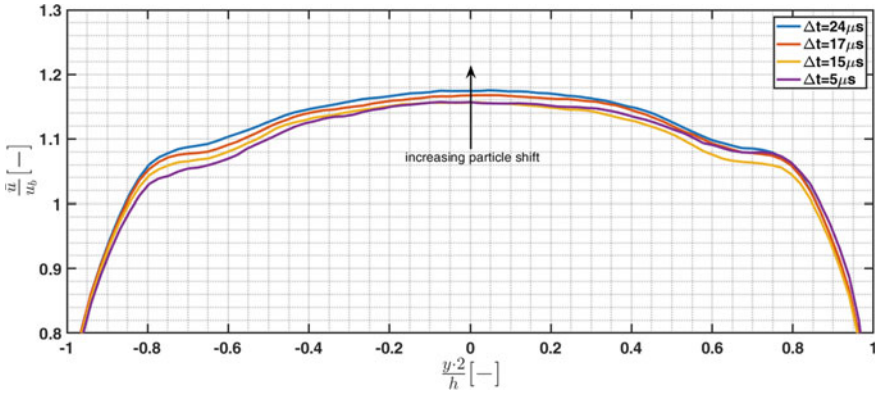

Fig. 8 Mean velocity profiles along the non-dimensional height of the duct, recorded with different laser pulse intervals

the rage of 3 px to 16 px. The particle shift mentioned is the maximum particle shift in the center of the duct. Figure 8 shows the mean velocity profile along the non-dimensional height of the duct. The profile is plotted for different laser pulse intervals at a Reynolds number of 52,000 based on the bulk velocity u_b and hydraulic diameter d_h of the cooling duct. It can be seen that the velocity gets higher with higher pulse intervals. The maximum difference between the highest and the lowest value is around 1.5%. However, both graphs with the smallest pulse interval seem to coincide in the center of the duct. Towards the edges appears some inconsistency. This inconsistency may be due to the tiny particle shift. Due to the lower velocity at the walls of the duct, the particle shift gets lower as well. Therefore, the particle movement can not be determined very well, and the measurement uncertainty arises. Nevertheless, a particle shift of around 10 px seems to be the best, due to the agreement in the center of the duct. The measurements with the higher Reynolds number of 105,000 are not shown here, because the results are very similar. A particle shift of 10 px is also verified as the best.

4 Conclusions

A lifetime experiment for rocket combustion chamber structures with an actively cooled, replaceable, and cyclically loaded fatigue specimen made of CuCr1Zr was developed. With an increasing number of load cycles the deformation of the hot gas wall is increasing nearly linearly. A critical value regarding the doghouse effect was found, which is almost independent from the loading. The slope of deformation per cycle is strongly dependent on the loading in terms of temperature gradient and level. The fatigue specimen has to resist three different phases during a load cycle, which cause different stress states in the hot gas wall. It can be concluded, that the

shutdown phase is damaging most, while creeping during the hot gas phase has a minor influence. Abrasion can be neglected. The use of thermal barrier coatings has decreased the lifetime. It is assumed that the influence of thermal aging is negligible. The fatigue experiment can be used for validation of numerical simulations regarding heat transfer and lifetime (e.g. [5, 17])

PIV measurements have been made in a generic high aspect ratio cooling duct. The results were analyzed well in terms of different parameters affecting the PIV measurements. It was shown that the results are repeatable and that the alignment with the micrometer screws is very accurate. PIV processing was analyzed to determine a proper setting. Furthermore, it turned out, that a particle shift of 10 px should be aimed for in this case. Therefore the laser pulse interval should be adapted in future measurements. With this preliminary study, the required PIV setup and the uncertainties are known well. A well-known reference measurement with a smooth wall is available now. These results are the starting point for the next analysis of the roughness effect on heat transfer and pressure loss in a high aspect ratio cooling duct.

Acknowledgements Financial support has been provided by the German Research Foundation (Deutsche Forschungsgemeinschaft – DFG) in the framework of the Sonderforschungsbereich Transregio 40.

References

1. Aharwal, K.R., Pawar, C.B., Chaube, A.: Heat transfer and fluid flow analysis of artificially roughened ducts having rib and groove roughness. Heat Mass Transf. **50**(6), 835–847 (2014)
2. Ahn, S.W., Son, K.P.: Friction factor and heat transfer in equilateral triangular ducts with surface roughness. KSME Int. J. **15**(5), 639–645 (2001)
3. Ahn, S.W., Son, K.P.: An investigation on friction factors and heat transfer coefficients in a rectangular duct with surface roughness. KSME Int. J. **16**(4), 549–556 (2002)
4. Anderson, W., Sisco, J., Sung, I.: Rocket combustor experiments and analyses. In: 14th Annual Thermal and Fluids Analysis Workshop (2003)
5. Barfusz, O., Hötte, F., Reese, S., Haupt, M.C.: Pseudo-transient 3d conjugate heat transfer simulation and lifetime prediction of a rocket combustion chamber. In: Future Space-Transport-System Components under High Thermal and Mechanical Loads (2020)
6. Fassin, M., Kowollik, D., Wulfinghoff, S., Reese, S., Haupt, M.C.: Design studies of rocket engine cooling structures for fatigue experiments. Arch. Appl. Mech. **86**(12), 2063–2093 (2016)
7. Fiedler, T., Rösler, J., Bäker, M., Hötte, F., Sethe, C.V., Daub, D., Haupt, M.C., Haidn, O., Esser, B., Gülhan, A.: Mechanical integrity of thermal barrier coatings - coating development and micromechanics. In: Future Space-Transport-System Components under High Thermal and Mechanical Loads (2020)
8. Hötte, F., Günther, O., Rohdenburg, M., Haupt, M.C., Scholz, P.: Roughness and crack investigations of rocket combustion chambers and pressure loss measurements in a high aspect ratio cooling duct. SFB TRR40 Annual Report (2019)
9. Hötte, F., Lungu, P., von Sethe, C., Fiedler, T., Haupt, M.C., Haidn, O.: Experimental investigations of thermo-mechanical fluid-structure interaction in rocket combustion chambers. J. Propul. Power **35**(5), 906–916 (2019)
10. Jankovsky, R., Arya, V., Kazaroff, J., Halford, G.: Structurally compliant rocket engine combustion chamber– experimental and analytical validation. J. Spacecr. Rock. **32**(4), 645–652 (1995)

11. Kandlikar, S., Joshi, S., Tian, S.: Effect of surface roughness on heat transfer and fluid flow characteristics at low Reynolds numbers in small diameter tubes. Heat Transf. Eng. **24**, 4–16 (2003)
12. Krogstadt, P.A., Andersson, H.I., Bakken, O.M., Ashrafian, A.: An experimental and numerical study of channel flow with rough walls. J. Fluid Mech. **530**, 327–352 (2005)
13. Quentmeyer, R.: Experimental fatigue life investigation of cylindrical thrust chambers. In: 13th AIAA/SAE Propulsion Conference, NASA-TM-X-73665 (1977)
14. Rang, H., Wong, T.T., Leung, C.: Effects of surface roughness on forced convection and friction in triangular ducts. Exper. Heat Transf. **11**, 241–253 (1998)
15. Thiede, R., Riccius, J., Reese, S.: Life prediction of rocket combustion-chamber-type thermo-mechanical fatigue panels. J. Propul. Power **33**(6), 1529–1542 (2017)
16. Hötte, F., Haupt, M.C.: Transient 3D conjugate heat transfer simulation of a rectangular GOX-GCH4 rocket combustion chamber and validation, Aerospace Science and Technology, Vol. **105**, (2020), https://doi.org/10.1016/j.ast.2020.106043
17. Hötte, F., von Sethe, C., Fiedler, T., Haupt, M.C., Haidn, O.J., Rohdenburg, M.: Experimental Lifetime Study of Regeneratively Cooled Rocket Chamber Walls, Int. J. Fatigue, Vol. 138, (2020), https://doi.org/10.1016/j.ijfatigue.2020.105649